Energy &
Environment Nexus

https://doi.org/10.48130/een-0026-0015

Rapid Report

Open Access

Controlled sulfidation of ternary transition metal towards high performance electrode materials for supercapacitors

Qing Pang, Hao Wu, Tengfei Wang, Boyu Liu and Hongyu Wang*

Received: 9 April 2026

Revised: 13 May 2026

Accepted: 15 June 2026

Published online: 4 August 2026

Abstract

Ternary transition metal sulfides (TTMS) are promising supercapacitor electrode materials, yet the influence of sulfidation on their phase evolution and electrochemical properties remains underexplored. In this study, controlled sulfidation of ternary transition metal hydroxides (TTMOH, NiCoFe-OH) is systematically investigated. Phase transitions from TTMOH to ternary transition metal oxides (TTMO, NiCoFe-O) and finally to TTMS (NiCoFe-S) are observed with increasing sulfidation temperature (35–115 °C). The NiCoFe-S_{95} electrode, featuring a TTMO/TTMS heterojunction, delivered optimal performance due to synergistic effects, achieving a capacity of 171.52 mAh g^{-1} at 2 mA cm^{-2}. It maintains 62.28% capacity after 10,000 cycles. This work provides critical insights into phase engineering for designing high-performance energy storage materials.

Keywords: Sulfidation, Electrode materials, Supercapacitors, Electrochemical performance

Highlights

- As temperature increases, the electrode material transforms from amorphous TTMOH to crystalline TTMO, and finally to crystalline TTMS.
- The introduction of Fe element is the main reason for the production of ternary transition metal oxides (TTMO).
- The crystalline TTMO/TTMS heterojunction electrode material exhibits excellent electrochemical performance.
- The obtained TTMO/TTMS heterojunction device demonstrates an energy density of 32.7 Wh kg^{-1} at 400 W kg^{-1}.

Introduction

With the development of renewable energy systems and electronic devices, efficient energy storage devices have become a core element of the energy transition[1]. Supercapacitors, with their high power density and fast charge-discharge capabilities, fill the technological gap between traditional batteries and capacitors[2]. However, their widespread application is limited by insufficient energy density[3]. Based on the key parameters that determine energy density, it is possible to maximize energy density by enhancing the voltage window and specific capacitance of electrode materials[4].

Ternary transition metal hydroxides (TTMOH) electrode materials, especially NiCo-based electrode materials, have become ideal candidates for a new generation of electrode materials due to their good structural stability, low cost, and excellent redox activity[5]. However, their low conductivity is an issue that cannot be ignored. As is well known, sulfur has low electronegativity[6]. Therefore, ternary transition metal sulfides (TTMS) exhibit higher conductivity, which in turn leads to superior electrochemical performance. For instance, Yan et al.[7] synthesized NiCoMn-LDH/NF on nickel foam (NF) via a hydrothermal method, followed by sulfidation to obtain NiCoMn-S/NF. Consequently, the optimized NiCoMnS/NF electrode demonstrated enhanced electrochemical performance compared to NiCoMn-LDH/NF, achieving a capacity of 872 C g^{-1} at 1 A g^{-1}. After 2,000 cycles, this electrode material maintains 87.7% capacity retention. Kumar et al.[8] synthesized NiCoZnS using a hydrothermal method. This electrode material exhibits a capacity of 1,171.3 C g^{-1} at 0.5 A g^{-1}. Furthermore, NiCoZnS retains 94.9% of its capacitance retention after 5,000 cycles. Among them, Mn and Zn ions exhibit similar issues, such as structural instability and a tendency to dissolve. Fe ions generally outperform other metal ions in terms of cycling stability and cost[9,10]. Therefore, constructing NiCoFe ternary transition metal compounds is beneficial for obtaining electrode materials with superior electrochemical performance. Liu et al.[11] synthesized Prussian blue materials combined with NiCoFe multi-metal composites via the co-deposition method. Subsequent sulfidation resulted in NCFS@PBA cubes. The ideal NCFS@PBA electrode demonstrates 1,644.4 F g^{-1} at 1 A g^{-1}. After 10,000 cycles, this electrode material maintains 89.1% capacity retention.

* Correspondence: Hongyu Wang (wanghongyu07010310@163.com)

Full list of author information is available at the end of the article.

https://doi.org/10.48130/een-0026-0015

Moreover, most researchers have only explored the morphology, phase, and electrochemical performance of the final transformation of TTMOH into TTMS, but have not conducted in-depth studies on the morphological transitions, phase structure composition, and corresponding electrochemical performance during this sulfidation process. For instance, Kang et al.[12] synthesized NiCoMn-OH via a hydrothermal method, used thioacetamide (TAA) as the sulfidation agent, and finally obtained NiCoMn-S by hydrothermal treatment at 120 °C for 4 h. Similarly, Tian et al.[13] loaded nickel-cobalt-zinc hydroxide (NiCoZn[OH]F) onto nickel foam (NF) through a hydrothermal method, employed Na_2S as the sulfidation agent, and obtained NiCoZnS by hydrothermal treatment at 120 °C for 12 h. Therefore, in order to better achieve controllable sulfidation and obtain electrode materials with superior electrochemical performance, it is crucial to investigate morphological transitions, phase structure composition, and corresponding electrochemical performance occurring during the sulfidation process.

Based on this, this paper first obtained TTMOH-NiCoFe-OH (NCF-OH) through the co-precipitation method and then controlled the hydrothermal temperature to obtain TTMS-NiCoFe-S (NCF-S) at different temperatures, thereby exploring the sulfidation patterns of the electrode material. The results show that as the hydrothermal temperature increases to 75 °C, the electrode material initially transforms from NiCoFe-OH to a ternary transition metal oxide (TTMO), namely TTMO-NiCoFe-O (NCF-O). As the temperature further increases, the electrode material gradually transforms into NCF-S. Among them, the electrode materials of NCF-S_{55} and NCF-S_{95} exhibit heterojunction structures of NCF-OH/NCF-O and NCF-O/NCF-S, respectively. The synergistic interaction of the two components results in an electrochemical performance that surpasses that of electrodes made from a single component. The specific capacities are 154.32 and 171.52 mAh g^{-1} at 2 mA cm^{-2}. An asymmetric supercapacitor (ASC) was fabricated using NCF-S_{95} and activated carbon (NCF-S_{95}//AC). At 1 A g^{-1}, it delivers a specific capacitance of 92 F g^{-1}. The energy density is 32.7 Wh kg^{-1} at 400 W kg^{-1}. After 7,000 charge–discharge cycles, the capacity retention rate of this ASC is 63.1%.

Experimental

Materials, characterization, and experimental methods are reflected in the supporting information.

Results and discussion

Structure characterization

Figure 1a schematically illustrates the structural evolution of the NCF-S electrode material during the preparation process. Initially, amorphous TTMOH nanosheets were obtained via co-deposition. Subsequent sulfidation at controlled temperatures (35–115 °C) yielded distinct crystalline phases. At 35 °C, the material retained its amorphous TTMOH nanosheet structure (Fig. 1b). Elevating the temperature to 55 °C induced partial crystallization, resulting in a heterojunction structure comprising amorphous TTMOH and crystalline TTMO, whose morphology was still nanosheet (Fig. 1c). Further increasing the temperature to 75 °C produced fully crystalline TTMO, and the nanosheets transformed into nanoparticles (Fig. 1d). According to Supplementary Fig. S1, at 75 °C, both Ni and Co monometallic transition metal hydroxides formed corresponding sulfides, while the Fe monometallic transition metal hydroxide existed in both oxide and sulfide forms, with the diffraction peak intensity of the oxide being significantly stronger than that of the sulfide. Therefore, it is concluded that the participation of Fe element leads to the formation of TTMO, and at 75 °C, the material did not reach the temperature required for complete sulfidation. At 95 °C, the material exhibited crystalline NCF-S (TTMS), forming a heterojunction with residual crystalline TTMO (Fig. 1e). At this temperature, the morphology transformed back to the nanosheet structure. Finally, at 115 °C, exclusively crystalline NCF-S (TTMS) was yielded, and its morphology remained a nanosheet structure (Fig. 1g). Collectively, these results demonstrate that progressively increasing the sulfidation temperature drives a sequential phase transformation: from the initial amorphous TTMOH to crystalline TTMO, and ultimately to crystalline TTMS. Concomitantly, the degree of sulfidation increases significantly with temperature.

The morphology evolution of the electrode materials with sulfidation temperature was investigated using SEM (Fig. 2). The precursor material was amorphous NCF-OH, which exhibited nanoparticle morphology formed by the agglomeration of small-sized nanosheets (Fig. 2a). At 35 °C, the size of the nanosheets increased (Fig. 2b). As the temperature rose to 55 °C, the nanosheets continued to grow in size (Fig. 2c). Notably, the morphology transformed into nanoparticles with significant agglomeration at 75 °C (Fig. 2d). This may be due to the oxidation reaction of the material. Further increasing the sulfidation temperature to 95 °C led to the reformation of nanosheet morphology. However, these nanosheets were significantly larger than those observed at 35 and 55 °C (Fig. 2e). In contrast, this material sulfided at the highest temperature (115 °C) is composed of relatively small nanosheets (Fig. 2f). The morphological changes of the electrode material with increasing hydrothermal temperature are consistent with the TEM results. Overall, sulfidation primarily produced nanosheet structures, except for the nanoparticle morphology observed at 75 °C (corresponding to the formation of NCF-O). Furthermore, the size of the nanosheets exhibited a non-monotonic dependence on temperature: it increased from 35 to 95 °C, then decreased at 115 °C, and reached the maximum dimensions at 95 °C. The EDS of the NCF-S_{95} sample (Fig. 2g) confirms the uniform spatial distribution of Ni, Co, Fe, O, and S on the nanosheet surface.

To investigate the changes in the phase of the electrode material as the sulfidation temperature increases, XRD analysis was conducted (Fig. 3a). The results showed that the phases of NCF-S_{35} and NCF-S_{55} were consistent with those of NCF-OH (JCPDS #40-0216), and the crystallinity of the electrode material gradually increased with the rise in sulfidation temperature (Supplementary Fig. S2a). However, NCF-S_{75} existed in the form of NCF-O, corresponding to JCPDS#04-005-6286 (Supplementary Fig. S2b). This is consistent with the TEM results. Meanwhile, NCF-S_{95} and NCF-S_{115} mainly existed in the form of NCF-S, corresponding to JCPDS #04-003-9607 (Supplementary Fig. S2c). It can be seen from Supplementary Fig. S3 that the amorphous NCF-OH does not have magnetism, and the samples obtained at hydrothermal temperatures of 35–55 °C do not exhibit magnetism. When the temperature rises to 75 °C, the sample exhibits strong magnetism, which is consistent with the NCF-O properties characterized by XRD. The sample at 95 °C also has strong magnetism. The pure NCF-S produced at the highest temperature (115 °C) does not have magnetism, which is also consistent with the NCF-S properties characterized by XRD. The results again show that NCF-S_{95} is a composite electrode material composed of magnetic NCF-O and non-magnetic NCF-S.

Additionally, XPS analysis of the electrode material can explore the changes in the valence states of surface elements as the sulfidation temperature increases. Figure 3b shows the full spectra of different electrode materials. It can be observed that the signals of Ni, Co, Fe, and O are detected in NCF-OH. As the electrode material undergoes further sulfidation, the S signal appears on the sample

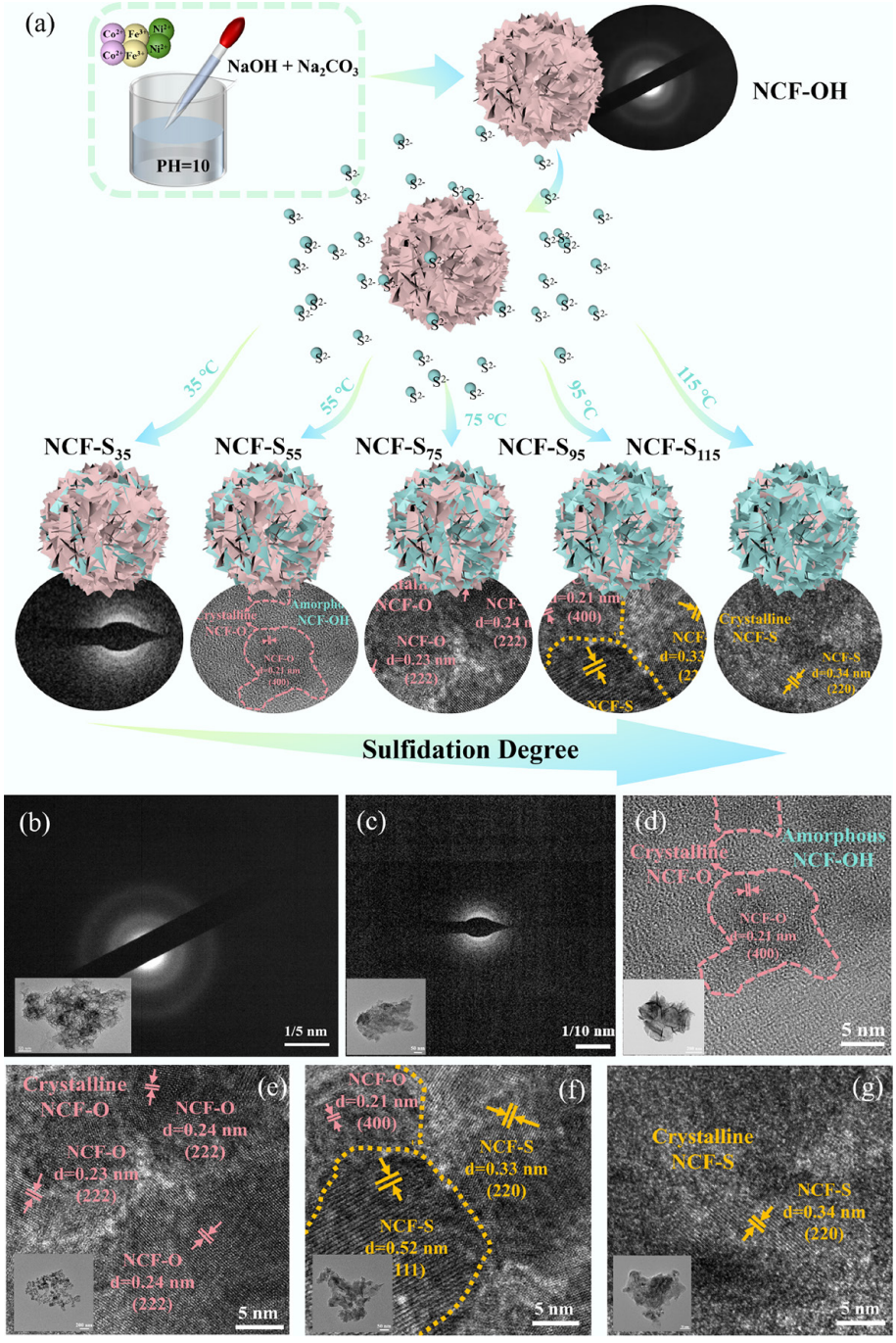

Fig. 1 (**a**) Preparation process diagram of NCF-S, SAED pattern images of (**b**) NCF-OH and (**c**) NCF-S_{35}, and TEM images of (**d**) NCF-S_{55}, (**e**) NCF-S_{75}, (**f**) NCF-S_{95}, and (**g**) NCF-S_{115}.

surface. Furthermore, with the increase in sulfidation temperature, the intensity of the S diffraction peak also increases, indicating a rise in the relative content of S in the electrode material, which in turn suggests an enhancement in the degree of sulfidation of the electrode material. This is consistent with the TEM results. It can be observed that Co initially exists in the form of Co^{2+}, with Co^{2+} $2p_{3/2}$ (781.2 eV) and Co^{2+} $2p_{1/2}$ (796.8 eV) (Fig. 3c)[14]. As the temperature increases to 75 °C, Co^{3+} begins to appear, with Co^{3+} $2p_{3/2}$ (778.2 eV) and Co^{3+} $2p_{1/2}$ (793.4 eV), and the Co^{2+} $2p_{3/2}$ and Co^{2+} $2p_{1/2}$ shift to 781.8 eV and 797.3 eV[15]. Ni initially exists in the form of Ni^{3+}, with the binding energies of Ni^{3+} $2p_{3/2}$ and Ni^{3+} $2p_{1/2}$ being 855.9 eV and 873.6 eV[16], respectively (Fig. 3d). Similarly, at 75 °C, Ni^{2+} starts to emerge, and the Ni^{3+} $2p_{3/2}$ and Ni^{3+} $2p_{1/2}$ peaks shift to 857.0 and 874.7 eV. However, due to the relatively low content of Ni^{2+}, only the diffraction peak of Ni^{2+} $2p_{3/2}$ (853.4 eV) was observed even when the temperature was raised to 115 °C (Supplementary Fig. S4)[17]. The two fitted peaks at binding energies of 714.7/711.5 eV ($2p_{3/2}$) and 727.4/724.6 eV ($2p_{1/2}$) correspond to Fe^{3+}/Fe^{2+} (Fig. 3e)[18]. For S, its spectrum exhibits two distinct peaks at 162.2 eV (S^{2-} $2p_{3/2}$) and 164.8 eV (S_2^{2-}) (Fig. 3f)[19–21]. At a temperature of 75 °C, a peak at 163.3 eV was observed, indicating that S^{2-} $2p_{1/2}$ began to appear with the increasing sulfur content. The diffraction peak appearing

https://doi.org/10.48130/een-0026-0015

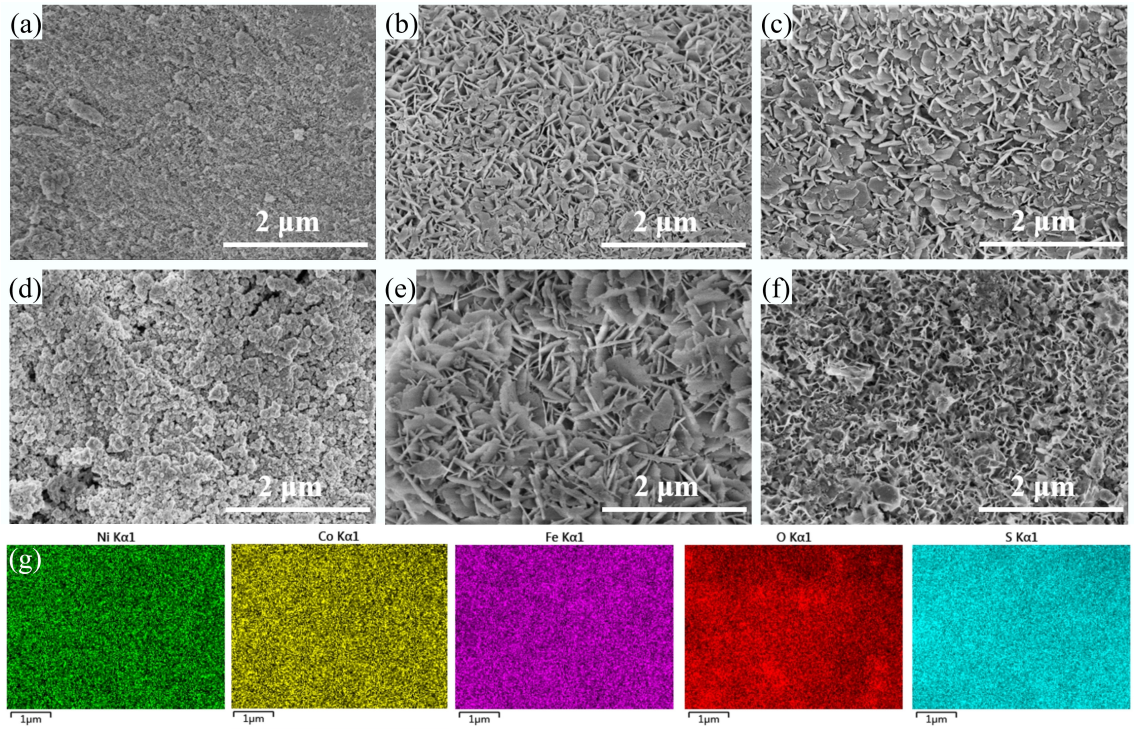

Fig. 2 SEM images of (**a**) NCF-OH, (**b**) NCF-S_{35}, (**c**) NCF-S_{55}, (**d**) NCF-S_{75}, (**e**) NCF-S_{95}, (**f**) NCF-S_{115}, and (**g**) EDS of NCF-S_{95}.

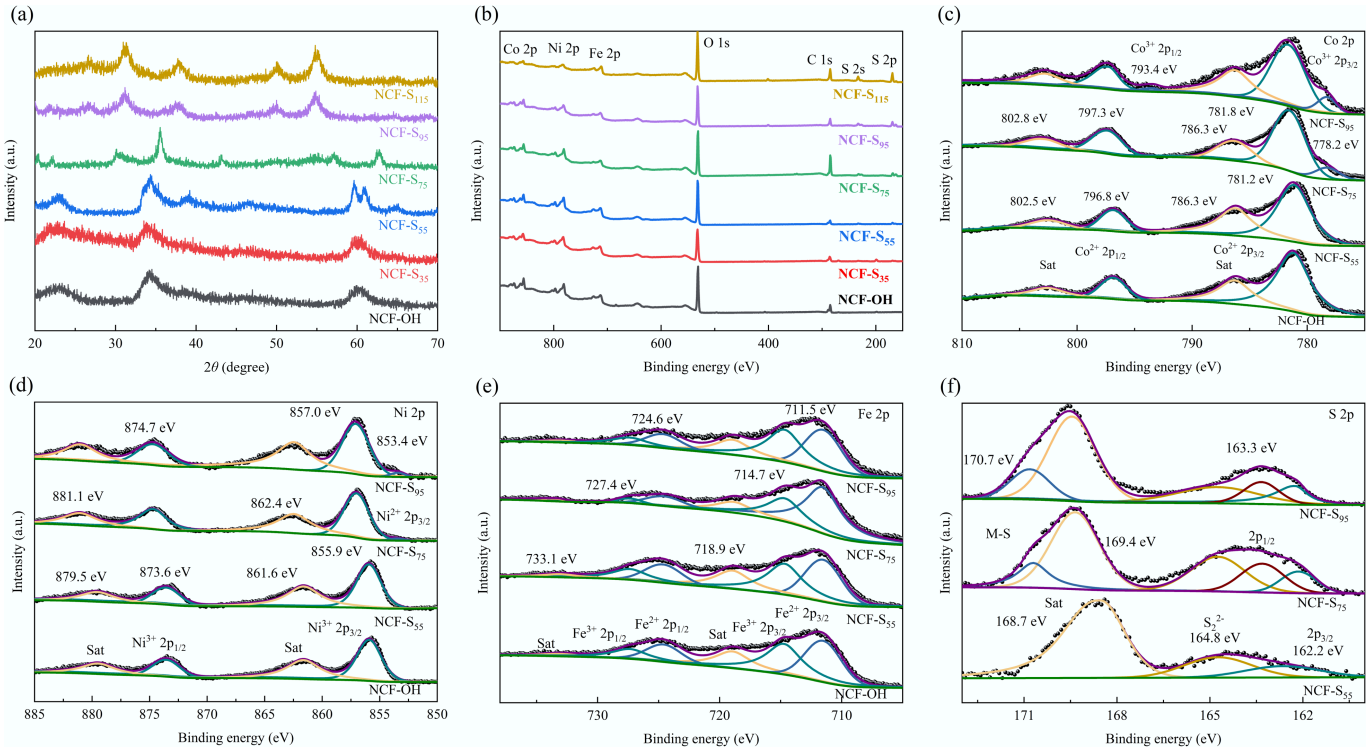

Fig. 3 (**a**) XRD pattern, (**b**) full spectrum, high-resolution spectra of (**c**) Co 2p, (**d**) Ni 2p, (**e**) Fe 2p, and (**f**) S 2p.

at 170.7 eV suggests the existence of M-S (M = Ni, Co, Fe) in the sample[22]. Meanwhile, O can be decomposed into three peaks corresponding to H_2O, M-OH, and M-O (M = Ni, Fe, Co), with binding energies of 532.7, 531.2, and 529.6 eV, respectively (Supplementary Fig. S5)[23]. It can be observed that as the temperature increases, the valence states of Co, Ni, and S on the surface of the electrode material undergo changes. At 75 °C, both Co^{2+} and Ni^{3+} begin to shift, which may be attributed to the transition from an amorphous to a crystalline state. As the atomic arrangement transforms from short-range disorder to long-range order, the local coordination environment of metal ions tends to become more uniform, and lattice defects are reduced[24].

Electrochemical characterization

Figure 4 displays the CV curves. All electrode materials exhibit a pair of distinct redox peaks, indicating that these materials are of the battery type (Fig. 4a). Moreover, NCF-S_{95} shows the largest enclosed area, suggesting superior electrochemical performance of this electrode material. Figure 4b presents the CV curves of NCF-S_{95}. With increasing scan rate, the enclosed area of curves expands. The appearance of these redox peaks originates from the Faradaic reactions between OH^- and Ni, Co, Fe, O, and S in the alkaline electrolyte[25,26].

$$(\text{Ni-Co-Fe})O_4 + H_2O + OH^- \leftrightarrow NiOOH + CoOOH + FeOOH + e^-$$

$$(\text{Ni-Co-Fe})S_4 + 3OH^- \leftrightarrow NiCoFeS_4(OH)_3 + 3e^-$$

Figure 4c compares the GCD curves of six electrode materials. All electrode materials exhibit discharge plateaus, and their charge–discharge curves are nearly symmetrical, indicating that the aforementioned materials behave as battery-type electrodes, which is consistent with the analysis of the CV curves. It can be observed that the voltage window of the electrode material exhibits a trend of first decreasing and then increasing. This indicates that the amorphous structure demonstrates a wider voltage window due to its disordered atomic arrangement, while an increasing degree of ordering leads to a reduction in the voltage window[24]. Additionally, sulfur's lower electronegativity facilitates rapid electron transfer, so as the degree of sulfidation increases, the voltage window of the electrode material gradually rises. According to Eq. (S1) in Appendix S1[27], specific capacitances of NCF-OH, NCF-S_{35}, NCF-S_{55}, NCF-S_{75}, NCF-S_{95}, and NCF-S_{115} are calculated to be 122.41, 141.25, 154.32, 148.15, 171.52, and 160.94 mAh g^{-1} at 2 mA cm^{-2}. The performance of sulfide electrode materials is better than that of NCF-OH, and the performance of heterojunction electrode materials is better than that of single-phase electrode materials. Amorphous TTMOH, due to its disordered internal structure, possesses rapid ion transport

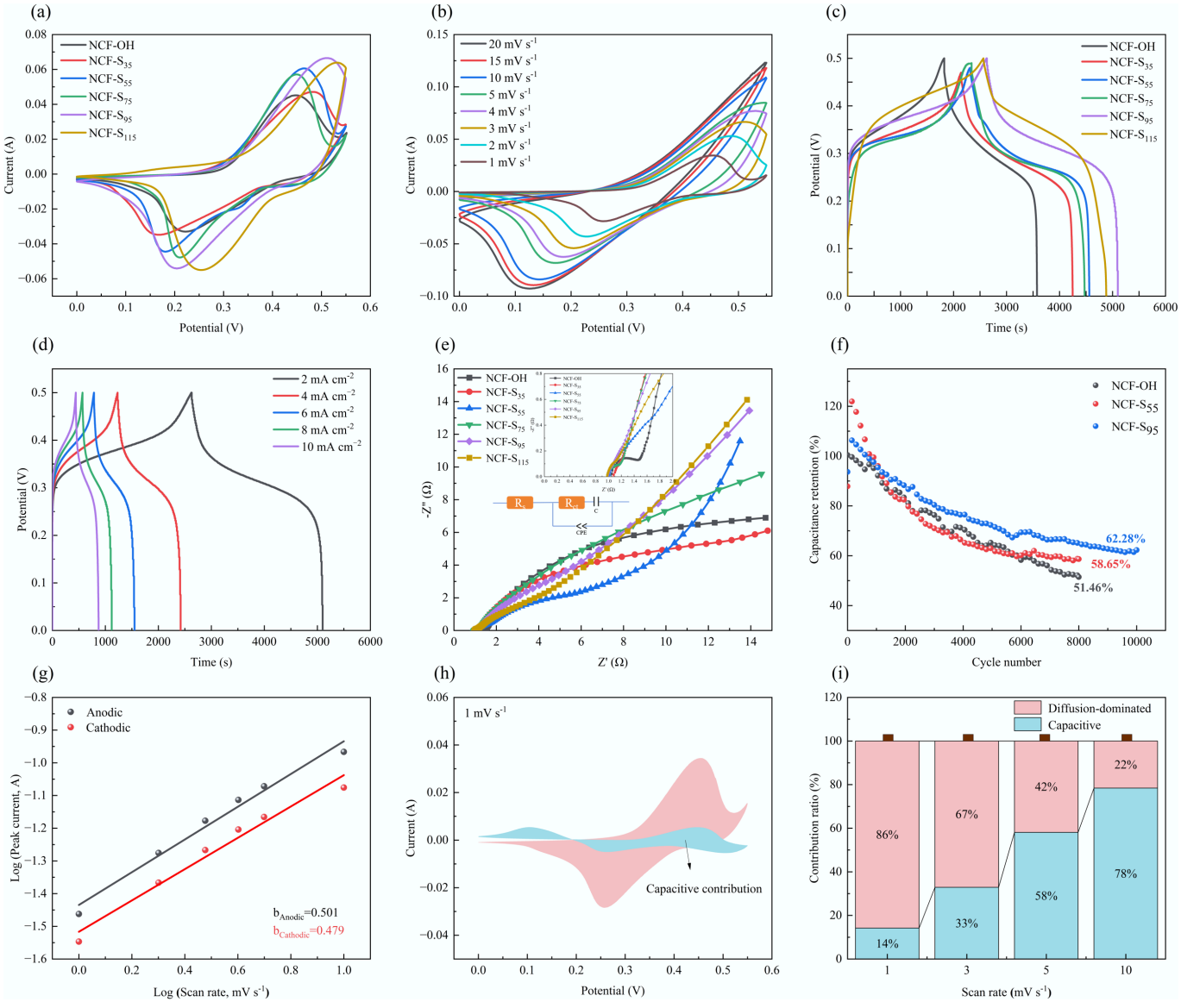

Fig. 4 (**a**) CV curves of different electrodes; (**b**) CV curves of NCF-S_{95}; (**c**) GCD curves; (**d**) GCD curves of NCF-S_{95}; (**e**) EIS curves; (**f**) cycle performance diagram; (**g**) b-value determination; (**h**) CV curve (shaded region) at 1 mV s^{-1} illustrating the capacitive and diffusion contributions. (**i**) Corresponding bar diagram for capacitive/diffusion contribution ratios of NCF-S_{95}.

https://doi.org/10.48130/een-0026-0015

channels but exhibits poor conductivity, whereas crystalline TTMO, with its ordered atomic arrangement, demonstrates relatively better conductivity. Therefore, the heterojunction electrode material (NCF-S_{55}) composed of TTMOH and TTMO combines favorable ion transport channels with electron transport channels. Additionally, its nanosheet structure provides a larger specific surface area compared to the nanoparticles of TTMO, enabling more extensive contact with the electrolyte. These two factors collectively contribute to the superior electrochemical performance of the NCF-S_{55} electrode material over single-phase electrode materials. As for the NCF-S_{95} electrode material, it consists of two components: crystalline TTMO and crystalline TTMS. Crystalline TTMO exhibits excellent structural stability, while crystalline TTMS possesses superior conductivity and electrochemical activity. TEM results reveal that the interplanar spacing of TTMS is slightly larger than that of TTMO, which facilitates ion transport. Consequently, this electrode material combines fast ion/electron transport channels with favorable electrochemical activity. The nanosheet structure also endows the material with a large specific surface area, enabling more sufficient contact with the electrolyte. These factors collectively contribute to the optimal electrochemical performance of the NCF-S_{95} electrode material. In addition, the electrochemical performance of NCF-S_{55} is lower than that of NCF-S_{115}, because NCF-S_{115} exists in the form of TTMS. Compared with hydroxides and oxides, sulfides have lower electronegativity of sulfur, which makes them have better electrochemical performance. Figure 4d shows the GCD curves of NCF-S_{95}. This electrode material retains 87.5% of its specific capacity at 10 mA cm^{-2}. Figure 4e presents the EIS curves of six electrode materials. The series resistances (R_s) are 1.06, 1.09, 1.05, 1.04, 1.01, and 1.02 Ω, and the charge transfer resistances (R_{ct}) are 0.37, 0.23, 0.31, 0.27, 0.21, and 0.24 Ω. The impedance of the electrode material after sulfidation is less than that before sulfidation. Due to the synergistic interaction of the TTMO and TTMS, the electronic/ionic conductivity is enhanced, resulting in the lowest impedance for NCF-S_{95}. Moreover, NCF-OH and NCF-S_{55} retained 51.46% and 58.65% of their initial capacity after 8,000 cycles. Furthermore,

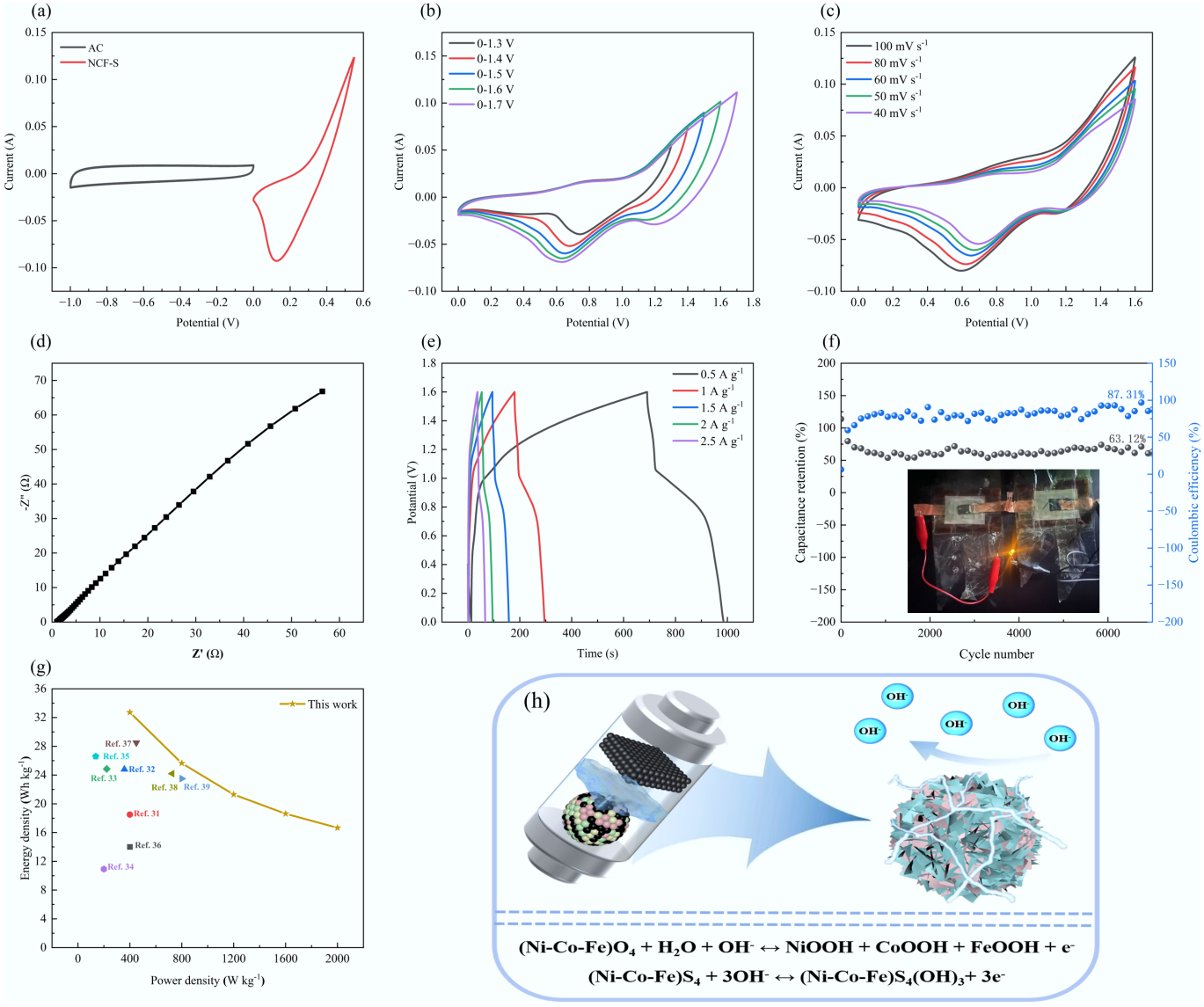

Fig. 5 (**a**) CV curves of NCF-S_{95} and AC; (**b**) CV curves in different potential windows; (**c**) CV curves at different scan rates; (**d**) EIS curve; (**e**) GCD curves; (**f**) cyclic stability; (**g**) electrochemical performance comparison diagram; (**h**) performance advantage diagram of NCF-S_{95}//AC.

NCF-S_{95} retained 62.28% of its capacitance after 10,000 cycles (Fig. 4f). This indicates that sulfidation improves the cycling performance. The constructed TTMO/TTMS heterojunction helps enhance cycling stability. Equation (S2) in Appendix S1[28] was employed to analyze the charge storage mechanism. For NCF-S_{95}, the b-values derived from the anodic and cathodic peaks are 0.501 and 0.479 (Fig. 4g), which indicate that its mechanism of charge storage is predominantly controlled by diffusion effects. A quantitative assessment using Eq. (S3) in Appendix S1[29] shows that at 1 mV s^{-1}, diffusion processes are dominant (Fig. 4h). Over the scan rate range of 1–10 mV s^{-1}, the capacitance contribution of NCF-S_{95} increased from 14% to 78% (Fig. 4i).

Electrochemical characterization of ASC

To evaluate the application potential of the electrode material, an ASC named NCF-S_{95}//AC was fabricated, with NCF-S_{95} serving as the positive electrode and AC as the negative electrode. The CV curves of the two individual electrodes are provided (Fig. 5a). NCF-S_{95} exhibits a voltage range of 0–0.55 V, while AC operates from −1 to 0 V. As seen in Fig. 5b, exceeding this voltage range (> 1.6 V) triggers the oxygen evolution reaction. Figure 5c displays the CV curves of NCF-S_{95}//AC at 40–100 mV s^{-1}. At high scan rates, the shape of the CV curve undergoes only minimal changes, indicating that NCF-S_{95}//AC possesses excellent reversibility. Figure 5d shows the EIS curve of NCF-S_{95}//AC, with R_s and R_{ct} being 1.06 and 0.44 Ω, respectively. Figure 5e presents the GCD curves of NCF-S_{95}//AC. The specific capacitance of the ASC is 92 F g^{-1} at 1 A g^{-1}. After 7,000 cycles, this ASC maintains 63.1% capacity retention. Additionally, by connecting two ASCs in series, an LED bulb can be illuminated for 14 min (Fig. 5f). According to Eqs (S4) and (S5) in Appendix S1 in the study by Korkmaz et al.[30], it can be calculated that the ASC has an energy density of 32.7 Wh kg^{-1} at 400 W kg^{-1}. Compared with reported devices, the performance of NCF-S_{95}//AC is better than that of the following supercapacitors (Fig. 5g)[31–39]. The aforementioned electrochemical test results indicate that the NCF-S_{95} electrode possesses high specific capacity and rate performance, which may be attributed to the synergistic effect between the TTMO and TTMS components (Fig. 5h). TTMO typically exhibits high structural stability and excellent cycling performance, while TTMS generally demonstrates higher theoretical specific capacity and superior ion diffusion kinetics. Therefore, the constructed TTMO/TTMS heterojunction not only integrates the inherent advantages of both materials but also forms a complementary effect. Meanwhile, the unique interface facilitates the acceleration of electron transport. In addition, NCF-S_{95} exists in the form of nanosheets, which have a larger specific surface area and better contact with the electrolyte than nanoparticles.

Conclusions

In summary, we successfully prepared the amorphous NCF-OH electrode material and observed its sulfidation behavior by regulating the sulfidation temperature. The NCF-S_{35} electrode material remained as amorphous NCF-OH. The NCF-S_{55} electrode material formed a heterojunction between amorphous NCF-OH and crystalline NCF-O. The NCF-S_{75} electrode material consisted solely of crystalline NCF-O. The NCF-S_{95} electrode material exhibited a heterojunction between crystalline NCF-O and crystalline NCF-S. Finally, the NCF-S_{115} electrode material consisted solely of crystalline NCF-S. With the increase in sulfidation temperature, the electrode material gradually transformed from the initial amorphous TTMOH to crystalline TTMO and finally to crystalline TTMS. The NiCoFe-S_{95} electrode material achieved a capacity of 171.52 mAh g^{-1} at 2 mA cm^{-2}. An ASC was constructed by combining NCF-S_{95} with AC (NCF-S_{95}//AC). At a power density of 400 W kg^{-1}, the energy density is 32.7 Wh kg^{-1}.

Supplementary information

It accompanies this paper at: https://doi.org/10.48130/een-0026-0015.

Author contributions

The authors confirm their contributions to the papaer as follows: Qing Pang: writing-original draft, methodology, investigation; Hao Wu: writing-original draft, methodology, investigation (same contribution as the first author); Tengfei Wang: methodology, investigation; Boyu Liu: methodology, investigation; Hongyu Wang: writing-review and editing, supervision, conceptualization. All authors reviewed the results and approved the final version of the manuscript.

Data availability

All the relevant data are available from the corresponding authors upon request. The data are not publicly available due to privacy or ethical restrictions.

Funding

The authors gratefully acknowledge the financial support from the Program of Science and Technology of Qinghai Province (No. 2024-ZJ-761).

Declarations

Competing interests

The authors affirm that there have no known competing financial interests or personal relationships that could have affected to influence the work presented in this paper.

Author details

Qinghai Provincial Key Laboratory of New Light Alloys, Qinghai University, Xining 810016, China

References

[1] Liu B, Wang T, Pang Q, Yang J, Liu H, et al. 2025. Enhancing the high-voltage electrochemical performance of Single-crystal $LiNi_{0.5}Co_{0.2}Mn_{0.3}O_2$ with mesoporous TiO_2 coating and Ti doping. *Ceramics International* 51:38141–38151

[2] Luo CW, Zhang K, Zeng HY, Wang HB, Xu KW, et al. 2025. Engineering oxygen vacancies into ZnCo hydrotalcite for boosting performances for flexible supercapacitor. *Journal of Power Sources* 633:236403

[3] Liu W, Chen Z, Ma Z, Li J, Liu Y, et al. 2024. High-load Ti_3C_2 MXene cathode through surface modification for degradable aqueous zinc-ion micro-supercapacitors with excellent energy density and anti-self-discharge. *Chemical Engineering Journal* 494:153149

[4] Wang H, Wang X, Liu X, Zhang S, Meng S, et al. 2025. High-performance Zn-ion hybrid supercapacitor based on 3D K^+-intercalated $Ti_3C_2T_x$ hydrogel cathode. *Journal of Alloys and Compounds* 1020:179588

[5] Zhao B, Zhang B, Lu C, Cai Z, Li L. 2020. Hierarchical hollow nanocages of Ni–Co amorphous double hydroxides for high-performance asymmetric supercapacitors. *Journal of Alloys and Compounds* 833:155130

https://doi.org/10.48130/een-0026-0015

[6] Zhang Y, Cai W, Guo Y, Wang Y. 2022. Self-supported Co-Ni-S@CoNi-LDH electrode with a nanosheet-assembled core-shell structure for a high-performance supercapacitor. *Journal of Alloys and Compounds* 908:164635

[7] Yan W, Zeng HY, Zhang K, Long YW, Wang MX. 2023. Ni-Co-Mn hydrotalcite-derived hierarchically porous sulfide for hybrid supercapacitors. *Journal of Colloid and Interface Science* 635:379–390

[8] Kumar AS, Sai KNS, Prasad K, Tighezza AM, Pabba DP, et al. 2024. *In-situ* constructed NiCoZnS composite on nickel foam with hierarchical structures as bifunctional electrocatalysts for oxygen evolution reaction (OER) and supercapacitors. *Journal of Alloys and Compounds* 1005:175983

[9] Wang Y, Ge W, Sun S, Guo Q, Shao R, et al. 2023. A hydrogel-assisting surface-confined corrosion strategy toward self-supported amorphous NiFe-layered double hydroxides enabling high-performance hybrid solid-state supercapacitors. *Journal of Energy Storage* 66:107473

[10] Phonsuksawang P, Khajondetchairit P, Butburee T, Sattayaporn S, Chanlek N, et al. 2020. Effects of Fe doping on enhancing electrochemical properties of $NiCo_2S_4$ supercapacitor electrode. *Electrochimica Acta* 340:135939

[11] Liu Q, Zhang J, Li Y, Nan W, Chen Z, et al. 2025. Discovered the enhanced mechanism of surface passivation for core–shell NiCoFeS@PBA cubes in electrochemical energy storage. *Chemical Engineering Journal* 509:161571

[12] Kang C, Ma L, Chen Y, Fu L, Hu Q, et al. 2022. Metal-organic framework derived hollow rod-like NiCoMn ternary metal sulfide for high-performance asymmetric supercapacitors. *Chemical Engineering Journal* 427:131003

[13] Tian ZF, Zeng HY, Lv SB, Long YW, Xu S, et al. 2022. Construction of NiCoZnS materials with controllable morphology for high-performance supercapacitors. *Nanotechnology* 33:245703

[14] Wu H, Zhang J, Lu Q, Li Y, Jiang R, et al. 2023. High-entropy layered double hydroxides with highly adjustable components for enhancing electrocatalytic oxygen evolution. *ACS Applied Materials & Interfaces* 15:38423–38432

[15] Zhu D, Wang K, Li X, Qi X, Jiang H, et al. 2024. Rose-like $NiCo_2O_4$ with atomic-scale controllable oxygen vacancies for modulating sulfur redox kinetics in lithium-sulfur batteries. *ACS Applied Materials & Interfaces* 16:17493–17505

[16] Wang J, Yang L, Fu Y, Yin P, Guan X, et al. 2021. Delicate control of crystallographic Cu_2O derived Ni-Co amorphous double hydroxide nanocages for high-performance hybrid supercapacitors: an experimental and computational investigation. *Nanoscale* 13:8562–8574

[17] Guo M, Li P, Wang A, Wang J, Chen J, et al. 2023. Topotactic synthesis of high-entropy sulfide nanosheets as efficient pre-catalysts for water oxidation. *Chemical Communications* 59:5098–5101

[18] Liang B, Ai Y, Wang Y, Liu C, Ouyang S, et al. 2020. Spinel-type $(FeCoCrMnZn)_3O_4$ high-entropy oxide: facile preparation and supercapacitor performance. *Materials* 13:5798

[19] Li Y, Li L, Du F. 2022. Amorphous S-doped $Ni_xCo_{3-x}O_4$ for high-performance asymmetric supercapacitors. *Electrochimica Acta* 434:141326

[20] Huang W, Dang S, Qu W, Gu R, Tian G. 2025. Coral-like cobalt-nickel sulfide/cobalt-nickel silicate composite with core-shell structure for hybrid supercapacitors. *Chemical Engineering Journal* 515:163271

[21] Huang B, Yuan J, Lu Y, Zhao Y, Qian X, et al. 2022. Hollow nanospheres comprising amorphous $NiMoS_4$ and crystalline NiS_2 for all-solid-state supercapacitors. *Chemical Engineering Journal* 436:135231

[22] Qiao X, Kang H, Wu J, Li Y, Wang Q, et al. 2019. A partial sulfidation approach that significantly enhance the activity of FeCo layered double hydroxide for oxygen evolution reaction. *International Journal of Hydrogen Energy* 44:31987–31994

[23] Wang T, Long X, Wei S, Wang P, Wang C, et al. 2020. Boosting hole transfer in the fluorine-doped hematite photoanode by depositing ultrathin amorphous FeOOH/CoOOH cocatalysts. *ACS Applied Materials & Interfaces* 12:49705–49712

[24] Joseph A, Mathew A, Thomas T. 2024. Effect of phase transformation on the electrochemical supercapacitive behavior of thermally exfoliated zirconia. *Journal of Energy Storage* 77:109969

[25] Zhang X, Zhang Z, Sun S, Wu Y, Sun Q, et al. 2018. A facile one-step hydrothermal approach to synthesize hierarchical core-shell $NiFe_2O_4$@$NiFe_2O_4$ nanosheet arrays on Ni foam with large specific capacitance for supercapacitors. *RSC Advances* 8:15222–15228

[26] Wang D, Wang J, Chu Y, Zha S, Chen Y, et al. 2024. Crystalline $NiCo_2O_4$ and amorphous $NiCo_2S_4$ heterostructured electrode for high-performance asymmetric supercapacitors. *Journal of Energy Storage* 96:112614

[27] Tang X, Wang J, Zhang D, Wang B, Xia X, et al. 2023. In-situ construction of carbon cloth-supported amorphous/crystalline hybrid NiCo-sulfide with permeable concrete-like morphology for high-performance solid-state hybrid supercapacitors. *Chemical Engineering Journal* 452:139429

[28] Chavan GT, Dubal DP, Morankar PJ, Jeon CW, An J, et al. 2025. Hierarchical CoMn-LDH and heterostructured composites for advanced supercapacitors and electrocatalysis applications. *Materials* 18:604

[29] Arif M, Riaz J, Yang H, Fu Z, Bibi A, et al. 2025. Synthesis of high-performance CdS/MnO composite electrode to achieve high energy and power densities for asymmetrical supercapacitors. *Materials & Design* 251:113704

[30] Korkmaz S, Kariper İA, Ceyran E, Kariper EB. 2025. Preparation of Co_3O_4 doped resorcinol formaldehyde xerogels and their supercapacitor performance. *Applied Physics A* 131:319

[31] Cheng X, Zhang L, Li L, Wu H, Zheng J, et al. 2025. One-step hydrothermal synthesis of Al-doped δ-MnO_2 with three-dimensional open network structure for high performance asymmetric supercapacitors. *Colloids and Surfaces A: Physicochemical and Engineering Aspects* 709:136163

[32] Ji F, Jiang D, Xia Q, Pan X, Chen X, et al. 2019. High-performance MoO_3 nanoplate electrode for asymmetric supercapacitor with long-term electrochemical stability. *Journal of Nanoscience and Nanotechnology* 19:5817–5824

[33] Zhu F, Liu W, Liu Y, Shi W. 2019. Self-supported hierarchical core–shell Co_9S_8@$NiCo_2O_4$ hollow nanoneedle arrays for asymmetric supercapacitors. *Inorganic Chemistry Frontiers* 6:982–987

[34] Hou JF, Gao JF, Kong LB. 2021. Enhancing the kinetic process in biphasic crystalline $NiWO_4$/amorphous Co-B electrode materials toward energy storage with ultrahigh rate performance. *Chemistry, an Asian Journal* 16:4130–4136

[35] Tao Y, Wu Y, Chen H, Chen W, Wang J, et al. 2020. Synthesis of amorphous hydroxyl-rich Co_3O_4 for flexible high-rate supercapacitor. *Chemical Engineering Journal* 396:125364

[36] Liu Y, Wen S, Shi W. 2018. Co_3S_4 nanoneedles decorated on $NiCo_2O_4$ nanosheets for high-performance asymmetric supercapacitors. *Materials Letters* 214:194–197

[37] Chen X, Wang S, Qiao G, Lu G, Cui H, et al. 2020. Fabrication of three-dimensional porous NiO/amorphous $Ni(OH)_2$ composites for supercapacitors. *Energy & Fuels* 34:16783–16790

[38] Liu WJ, Yuan M, Lian JB, Li GC, Li QP, et al. 2023. Embedding partial sulfurization of iron–cobalt oxide nanoparticles into carbon nanofibers as an efficient electrode for the advanced asymmetric supercapacitor. *Tungsten* 5:118–129

[39] Zhou Y, Jia Z, Zhao S, Chen P, Wang Y, et al. 2021. Construction of triple-shelled hollow nanostructure by confining amorphous Ni-Co-S/crystalline MnS on/in hollow carbon nanospheres for all-solid-state hybrid supercapacitors. *Chemical Engineering Journal* 416:129500